Eurographics Conference on Visualization (EuroVis) 2013
B. Preim, P. Rheingans, and H. Theisel
(Guest Editors)

Volume 32 (2013), Number 3

AmniVis - A System for Qualitative Exploration of Near-Wall Hemodynamics in Cerebral Aneurysms

M. Neugebauer†[1], K. Lawonn[1], O. Beuing[2], P. Berg[3], G. Janiga[3] and B. Preim[1]

[1]Department of Simulation and Graphics, University of Magdeburg, Germany
[2]Department of Neuroradiology, University Hospital Magdeburg, Germany
[3]Institute of Fluid Dynamics and Thermodynamics, University of Magdeburg, Germany

Abstract

The qualitative exploration of near-wall hemodynamics in cerebral aneurysms provides important insights for risk assessment. For instance, a direct relation between complex flow patterns and aneurysm formation could be observed. Due to the high complexity of the underlying time-dependent flow data, the exploration is challenging, in particular for medical researchers not familiar with such data. We present the AmniVis-Explorer, a system that is designed for the preparation of a qualitative medical study. The provided features were developed in close collaboration with medical researchers involved in the study. This comprises methods for a purposeful selection of surface regions of interest and a novel approach to provide a 2D overview of flow patterns that are represented by streamlines at these regions. Furthermore, we present a specialized interface that supports binary classification of patterns and temporal exploration as well as methods for selection, highlighting and automatic 3D navigation to particular patterns. Based on eight representative datasets, we conducted informal interviews with two bord-certified radiologists and a flow expert to evaluate the system. It was confirmed that the AmniVis-Explorer allows for an easy selection, qualitative exploration and classification of near-wall flow patterns that are represented by streamlines.

Categories and Subject Descriptors (according to ACM CCS): I.3.6 [Computer Graphics]: Methodology and Techniques, Interaction Techniques—I.3.8 [Computer Graphics]: Applications—

1. Introduction

Cerebral aneurysms, abnormal local dilatations of arterial intracranial vessels, are caused by structural weakening of the stabilizing layer of the vessel wall. A rupture can lead to a subarachnoid haemorrhage. The resulting interruption of blood support and the fast accumulation of blood in the ventricular system lead to a high fatality rate of 45%-75% [RRW*08]. The number of unintentionally detected cerebral aneurysms is rising due to an increase of cerebral scans and the general improved imaging quality. However, the treatment of aneurysms is also fraught with risks, like vascular occlusion or even a rupture [MKB*09]. This emphasizes the need for a differentiated assessment of the risk of rupture.

Studies have shown that hemodynamic discriminants, acquired through computational fluid dynamics (*CFD*), are essential for risk assessment [XNT*11]. Among the potentially relevant quantitative hemodynamic parameters is the wall shear stress (*WSS*) [CMWP11b]. However, while there is a relation between *WSS* and its derivatives and the risk of rupture, it is still not clear which amount of *WSS* will cause a rupture. This is probably due to the often heterogenic aneurysm wall thickness [KDM12]. Another approach to risk assessment is based on a qualitative analysis of the hemodynamics. A relation between complex flow patterns and aneurysm formation and growth could be observed. Those qualitative findings also form the basis for a more sophisticated quantitative analysis of hemodynamics [CMWP11a].

Currently, our medical partners prepare a study that involves the comparative, qualitative analysis of near-wall hemodynamics of selected cases. These include rare datasets of aneurysms with known rupture site. They were acquired just before the rupture occurred. Also included are datasets con-

† mathias.neugebauer@ovgu.de

taining multiple aneurysms, one of which caused a small bleeding. For preparation of the study, medical experts are currently screening the datasets and try to identify salient near-wall flow patterns, while elaborating the definition of salient flow patterns.
This procedure involves the selection of wall regions of interest (*ROI*), the visualization of flow at these *ROI*s and the visual comparison and subsequent classification of the flow patterns over time. We developed the AmniVis-Explorer to support these tasks with appropriate visualization and interaction schemes. Its central features as well as the main contributions of this paper are:

- Automatic selection of *ROI*s, automatic seeding and parameterization for streamline-based flow visualization
- A 2D overview representation of the flow patterns with a layout that supports manual binary classification
- Convenient interaction: selective highlighting and guided 3D navigation through automatic camera positioning

2. Related Work

A broad range of visualization techniques is available for the qualitative exploration of hemodynamics. According to the general flow visualization literature, they can be categorized into dense, feature- and integration-based approaches [PVH*03] [MLP*10].
There are several examples for the application of integration-based approaches and specific seeding-strategies in the field of hemodynamic visualization. Rosanwo et al. employ dual streamline seeding that allows for uniform coverage of the surface flow of a cerebral aneurysm [RPP*09]. However, this approach is restricted to the surface, without conveying the volumetric nature of near-wall flow. Pelt et al. emphasize certain sections of intravascular flow through seeding patterns on interactive, orthogonal probing planes [vPBB*10]. Putting the focus on anatomic features, Neugebauer et al. employ the ostium as seeding region to visualize only flow that circulates through the aneurysm [NJB*11].
To represent near-wall flow, similar seeding strategies can be applied to the surface of the aneurysm. Köhler et al. describe an approach for the manual placement of seed regions on the aneurysm wall [KNG*12]. To automatically place these regions, we need a surface metric. Studies show that aneurysms with blebs and a general increased curvature also exhibit a higher risk of rupture [MFW*05]. Thus, surface areas with increased curvature are assumed to be predestined for locating salient flow patterns. The detection of curvature-based features was explored in colonoscopy [YD04]. Yoshida et al. detect polyps based on two curvature measures: the shape index and the curvedness [DJ97]. We analogously employ these measures to find aneurysm surface locations that are suitable for seeding.
An adequate streamline rendering and viewpoint selection is crucial for a correct spatial interpretation of flow represented by streamlines. Gasteiger et al. present a set of illustrative rendering techniques to support a simultaneous depiction of surface and underlying flow [GNBP11]. We employ a related rendering style. Mühler et al. describe a general approach on good viewpoint selection for medical visualizations [MNTP07] while Tao et al. focus on selection of optimal viewpoints for streamline-based flow visualizations [TMWS12]. However, since we concentrate on near-wall flow, it is sufficient to derive the viewpoint from surface parameters.
To provide an overview, we employ 2D representations of the near-wall flow patterns by flattening the streamlines. There are comparable surface-based approaches. Neugebauer et al. provide an interactive flat representation of scalar aneurysm surface flow data based on cube mapping [NGB*09]. However, the inherent distortion does not relate to the underlying flow. Petz et al. reduce this distortion by flattening surface patches with low initial curvature [PPG*08]. However, since we seed in areas with high curvature a flow pattern would be presumably represented by several patches.

3. Explorer Features and Supported Tasks

The features of the AmniVis-Explorer are directly derived from the data used in the planned study, the central study tasks and the user group performing the study. In the following we outline the relation between the study and the explorer features; details on the specific implementation are given in the following sections.

Data-driven features. The study will focus on the identification of salient near-wall flow patterns close to preselected wall *ROI*s. Thus, the AmniVis-Explorer needs to provide mechanisms to visualize near-wall flow. Feature-based approaches often need a quantitative description of the flow features of interest, which is not yet given in our field of application. Dense, texture-based approaches, like *LIC*, are suitable for 2D flow or planar cross sections of 3D flow. Even though the wall *ROI*s exhibit a planar layout, the near-wall flow is volumetric and could not be represented without occlusion. In contrast, integration-based approaches provide a sparse, volumetric representation of the flow. They also allow for a spatial flow selection through the integration length and the definition of a seeding region. Therefore we decided to employ an integration-based method to visualize near-wall flow patterns.
Our medical partners are interested in basic, non-derivative flow parameters like direction and velocity. Those can be visually encoded by line-based flow representation. Thus, we concentrate on integration-based methods resulting in lines, rather than surfaces or high-dimensional structures with a corresponding higher visual complexity. The visualization can be focussed on the spatial (streamlines) or temporal (pathlines) components of the underlying data. From discussions with our medical partners, we learned that the spatial component is of major interest. They want to understand

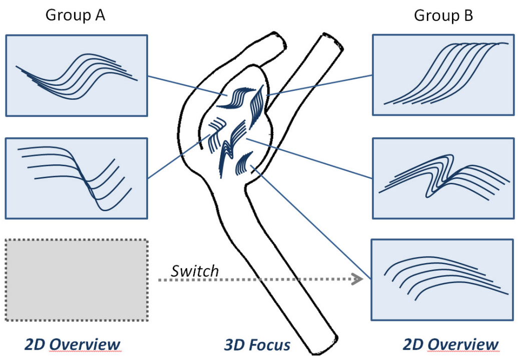

Figure 1: *Mock-up of the AmniVis-Explorer layout: The 2D representations of the streamline bundles provide an overview. Their vertical arrangement left and right of the 3D focus represents the classification.*

which patterns occur at specific points in time (e.g. diastolic peak) at specific locations close to the wall. Thus, we eventually decided to employ streamlines to visualize the near-wall flow.

Task-driven features. The studies' central tasks will be the selection of *ROI*s and the visual comparison of flow features present at these *ROI*s in order to derive some kind of classification. The selection of seeding regions can be tedious, e.g. involving complex 3D navigation in order to visually inspect the surface. We learned that potential *ROI*s are locally elevated, cap-shaped surface areas. Thus we employ a specific surface metric to automatically identify these areas and create comparable seeding regions. However, since there might occur additional, non-quantified selection parameters it should be possible to manually alter this selection.

Due to their integration-based nature, the flow patterns can be qualitatively compared based on their shape. However, they are volumetric and can be distributed everywhere below the aneurysm wall. Thus, a visual comparison would at least be as tedious as the aforementioned surface inspection. An overview showing all patterns allows for comparison without 3D navigation. However, this overview must represent the flow patterns in a comparable fashion irrespective of local pattern orientation. Thus, we flatten each pattern with respect to the adjacent vessel wall and orient the resulting 2D representation with respect to the underlying flow direction. This dimensional reduction also allows for convenient temporal overview by presenting different points in time side by side.

However, due to the introduced distortion, this overview should function as contextual information; the final decision should be derived from the 3D representation of the pattern. This requires a seamless integration of 2D contextual overview and 3D flow visualization in the final explorer layout. Additionally, the 2D overview also serves as part of the user interface, e.g. to highlight a certain pattern. As comparison and binary classification are closely related tasks, we choose the layout of the 2D overview to support both (see Fig 1). Classification is performed by either arranging a 2D pattern representation at the left or right side of the screen.

User-driven features. The neuroradiologists preparing the study are not familiar with creating or navigating complex 3D visualizations. Thus, the visualizations provided by the explorer need to be parameterized automatically. This includes the creation of seeding regions and seed point distribution, the streamline integration and the general visualization of surface, 3D streamlines and 2D representations. The necessary parameters are derived from the underlying dataset, employing pre-defined templates. For 3D navigation we provide automatically generated viewpoints and camera paths.

4. Data Acquisition and Preprocessing

To enable near-wall seeding, a polygonal representation of the vascular wall is extracted from image data. As computational domain the CFD simulation employs a volumetric mesh that is derived from the polygonal surface. To focus the exploration on the area of interest, the aneurysm is automatically separated from the adjacent vasculature.

Wall representation. We employ angiographic image data from Computed Tomography Angiography (*CTA*) or Magnetic Resonance Angiography (*MRA*). Due to contrast agents or special sequences, the vessel lumen exhibits a high contrast, leading to a good signal-to-noise ratio. In most cases, a threshold-based segmentation with a subsequent isosurface extraction (*Marching Cubes*) is sufficient to obtain a polygonal representation. In cases of low image quality, a deformable model is employed [LABFL09]. To ensure anatomical plausibility, the results are evaluated by our medical partners.

Simulation. We improve the polygonal surface quality through an advancing fronts remeshing and subsequent topological changes (for details we refer to [Sch97]). From this, a hybrid volume mesh is generated with three prismatic layers at the wall, allowing for a finer resolution of velocity gradients. The unstructured inner volume is made of tetrahedral elements, with a spatial resolution that is adequate for resolving occurring vortices. The inflow conditions for the unsteady simulation are derived from image-based flow measurements (7 Tesla PC-MRI) of healthy volunteers. Blood is considered to be a Newtonian fluid and the walls are assumed to be rigid, which is adequate with respect to the application domain (cerebral arteries with $< 5\%$ radial variation over the cardiac cycle).

Aneurysm separation. The ostium, a planar representation of the in-/outflow area, is employed to separate the aneurysm from the adjacent vasculature. We employ an automatic approach to generate a polygonal representation of the ostium. For a detailed description we refer to [NDSP10].

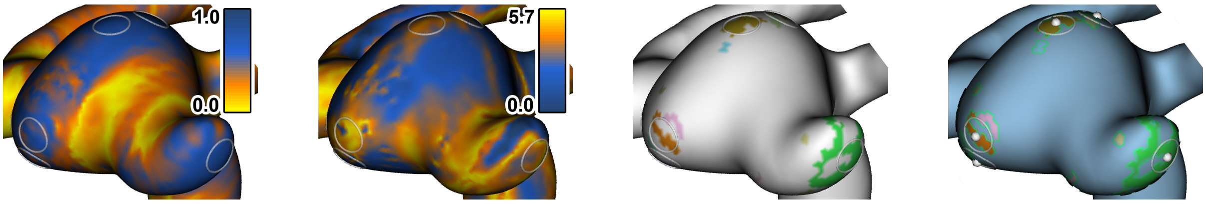

(a) Shape index (b) curvedness (c) Connected components (d) Circular seeding regions

Figure 2: *The selection of the* ROIs *based on shape index and curvedness. A shape index threshold (> 0.9 - cap shape) leads to connected components. Circular seeding region are created from an importance-dependent subset.*

5. ROI Selection and Seeding

We employ the shape index and the curvedness to identify *ROI*s on the aneurysm surface that are shaped like caps. Circular seeding regions at these *ROI*s form the basis for the subsequent streamline integration. This is an automatic process; all parameters are derived from the dataset.

ROI selection. Analogous to the work presented in [YD04] we employ the shape index and the curvedness to identify *ROI*s. Cap-shaped areas resemble the blebs and local curvature deviations our medical partners are interested in. The surface shape at point p can be quantified with the shape index s:

$$s(p) = \frac{1}{2} - \frac{1}{\pi}\tan^{-1}\frac{\kappa_1(p)+\kappa_2(p)}{\kappa_1(p)-\kappa_2(p)}$$

with κ_1 and κ_2 being the principal curvatures and $\kappa_1 \geq \kappa_2$. The shape index ranges from 0 (cup) to 1 (cap). Flat shapes with $\kappa_1 = \kappa_2 = 0$ are not defined and symbolically labelled with -1. The cap shape we are interested in has a shape index $s \geq 0.9$. The shape index is sensitive to cap shapes of all scales. To restrict the *ROI*s to local caps rather than the overall bulges, the aneurysms consists of, we also quantify the scale of the local curvature with the curvedness c:

$$c(p) = \sqrt{(\kappa_1^2(p)+\kappa_2^2(p))/2}$$

with c raising with an increased local curvature, starting from 0 at flat areas. We compute the mean curvedness c_{mean} for the aneurysm domain. Thus, all surface areas with $c > c_{mean}$ exhibit a curvature above average and are potential *ROI*s. If they also have a shape index $s \geq 0.9$, we mark them as *ROI*. After this thresholding, a connected component analysis is employed to identify singular *ROI*s (see Fig. 2(c)). To define the importance of each *ROI* we use the maximum curvedness of each connected component. In order to reflect the assumed relation between blebs and a raised risk of rupture, *ROI*s with a higher curvedness are ranked as more important than flatter *ROI*s.

Circular seeding region. To support comparability of the flow patterns, we employ circular seeding regions (*CSR*s) rather than seeding from the variably formed *ROI*. The center of a sphere is positioned at the point of the *ROI* that has the maximum curvedness. All aneurysm vertices within the sphere are assigned to the corresponding *CSR*. To also support comparability in-between different datasets, the radius of the *CSR*s is derived from the aneurysm size. In order to quantify the aneurysm size, we approximate the aneurysm with a triaxial ellipsoid. The ellipsoids axes are the eigenvectors scaled by the eigenvalues of the covariance matrix of all aneurysm vertices. The mean length L_a of all three axes approximates the mean diameter of the aneurysm. As parameter recommendation, the *CSR* radius is set to be $r = L_a/6$. This corresponds to circular regions with a polar diameter of 20° on a sphere, which was assessed to be adequate by our medical partners.
Since we want to integrate the near-wall flow, the seed points are placed below the surface triangles of a given *CSR*. The distance between the seed points and the aneurysm surface is derived from the hybrid simulation volume mesh, since it provides information about the resolution of the simulation data. To allow for a higher sampling rate, flow close to the wall is represented through three prismatic layers. We position the seed points in the middle of the second layer.
To allow for a tessellation-independent seed point distribution, each *CSR* triangle has an area-dependent probability that a seed point will be placed there. Seed points are more likely to be placed at larger triangles. The seed points are uniformly distributed within the triangle domain. To ensure an adequate flow sampling, we want an average of four seed points per triangle. Thus, the overall number of seed points n_s for a *CSR* is derived from the mean area of the *CSR* triangles A_{mean} and the area of the *CSR* A_{CSR} with $n_s = (A_{CSR}/A_{mean}) \cdot 4$.

Automation levels. For an automatic selection, a user selected number of *CSR*s with respect to their ranking is provided. The semi-automatic selection neglects the ranking and requires the user to select a subset from all potential *CSR*s. The manual selection does not involve the surface metric. The user selects a vertex which is used as center for a corresponding *CSR*. The parameter recommendations for all selection steps can be interpreted as a template. They match the preferences of our medical partners but can easily be altered with respect to different requirements, while still depending on the underlying dataset.

6. Generation of Local Flow Representations

The flow pattern at each *CSR* is represented by streamlines. The overview of all flow patterns relies on 2D representations based on unrolled streamlines. The necessary parameters for integration and flattening of the streamlines are derived from the dataset.

Streamline tracing. A fourth order Runge-Kutta integrator is used for bidirectional streamline integration. The maximum propagation length L_p is the parameter that influences how much of the underlying flow field is represented. Based on discussions with our medical partners, L_p is derived from the size of the aneurysm. As described in Section 5, we employ the mean length L_a of the approximated local aneurysm axes as size indicator for the aneurysm. A propagation length of $L_p = L_a/1.7$ was assessed to be adequate. This is equivalent to a polar diameter of 70° on a sphere. Thus, the streamlines represent the flow surrounding the current *CSR* without too much interference with other *CSR*s for most of the cases. As with the parameters presented in the previous section, this is a template that can be altered if the requirements change.

Unrolled streamlines. We need a planar domain to create a 2D representation of the streamlines. For this, we employ a plane derived from the *CSR*. The normal n_{CSR} of this *CSR*-plane equals the mean of all *CSR* vertex normals. The origin equals the center of the *CSR*.

Each streamline S_i of the streamline bundle at a given *CSR* consists of linearly connected points $S_i = \{p_0, p_1, ..., p_k\}$ where p_0 equals the seed point. As algorithm initialization, p_0 is orthogonally projected into the *CSR* plane and the remaining points of S_i are shifted accordingly. The unrolling algorithm is based on iterative rotations of subsets of the streamline points. Given a point p_l that already lies on the plane (initially $p_l = p_0$), a rotation around this point is used to map the consecutive point p_{l+1} into the *CSR* plane. To obtain a suitable rotation axis, we orthogonally project p_{l+1} into the plane, leading to the projected point p'_{l+1}. Let $d = p'_{l+1} - p_l$ be the points' direction vector in plane space. Our rotation axis is defined as: $a_{rot} = (d \times n_{CSR}) / \|d \times n_{CSR}\|$. Furthermore, let α be the angle between $p_{l+1} - p_l$ and $p'_{l+1} - p_l$. All consecutive points p_{l+i} are rotated around p_l, with the rotation axis a_{rot} and the rotation angle α. Thus we get:

$$p^{New}_{l+i} = Q \cdot \left(p^{Old}_{l+i} - p_l\right) + p_l$$

with Q being the rotation matrix. After all points are processed, we obtain a streamline that lies in the *CSR* plane. Since the rotation matrix is an isometry, it is length- but not necessarily angle-preserving. However, given the angle β between two consecutive linear segments of the streamline, at least the angular component parallel to the *CSR* plane is preserved. Thus, parts of the streamline that are parallel to *CSR* plane are more faithfully represented with respect to angle distortion (see Fig. 3). Streamlines close to the *CSR* often exhibit this parallel orientation, whereas the sections at the far ends often bow away due to the convex aneurysm shape. Thus, the flow at the *CSR* center tends to be represented with higher accuracy. This is sufficient for a contextual representation. Since there is an implicit relation between the grade of distortion and the distance of the original streamline to the *CSR* plane, it is employed as qualitative reliability indicator when visualizing the unrolled streamlines. Due to the lack of quantification, this is not a representation of uncertainty or distortion but a visual hint, suitable for contextual application.

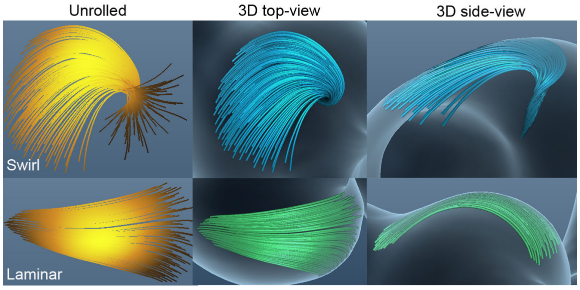

Figure 3: *The distortions in the 2D representation get stronger (dark brown), if the streamlines bend into the aneurysm. Sections close to the CSR plane (yellow) are represented less distorted.*

7. The Explorer -Layout, Visualization and Interaction

The AmniVis-Explorer layout is based on a focus-context strategy. The streamlines and unrolled streamlines are created for every time step and employed for the explorer's qualitative focus and context visualization respectively. Due to the spatially faithful representation of the flow, the decision whether a pattern is salient is made based on the 3D focus. However, the 3D visualization exhibits drawbacks: a high mental effort to gain an overview of all patterns, especially concerning their change over time, a high rate of mutual occlusion, and tedious comparison due to inconsistent pattern orientation.

To address these issues, the unrolled streamlines are employed as context (see Fig. 4). Their planar layout allows for a consistently oriented, simultaneous visualization of multiple patterns and time steps. Besides serving as overview, the context visualization also serves as the explorer interface.

The unrolled streamlines are integrated in *streamline widgets*. Each widget also contains control elements to highlight and automatically navigate to the corresponding 3D focus streamlines, to change the represented time step of the pattern, and to enable a temporal overview that includes several time steps (*timeline view*).

The main task, the binary classification, is realized through the widget's arrangement. Initially, the widgets are vertically arranged at the left side, in descending order according to the rank of the corresponding *CSR*. If a user decides, that a par-

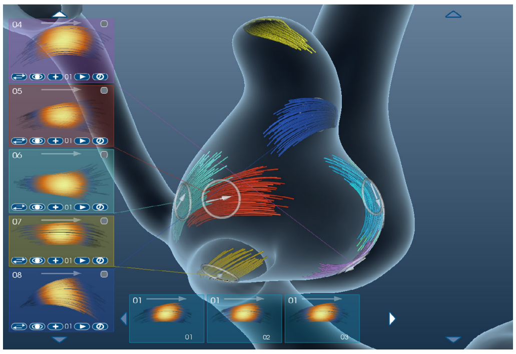

(a) Initial state

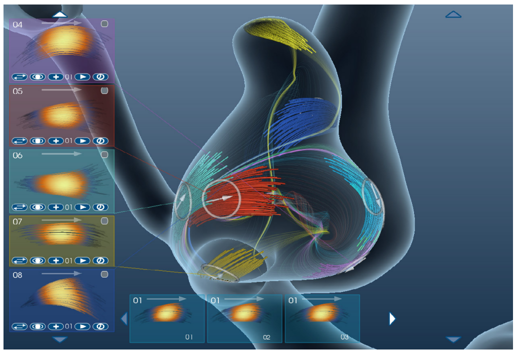

(b) Spatial context

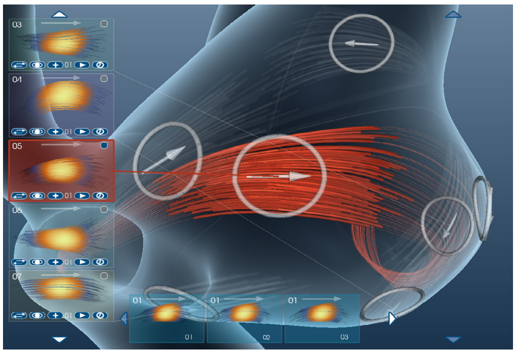

(c) Navigation & selection

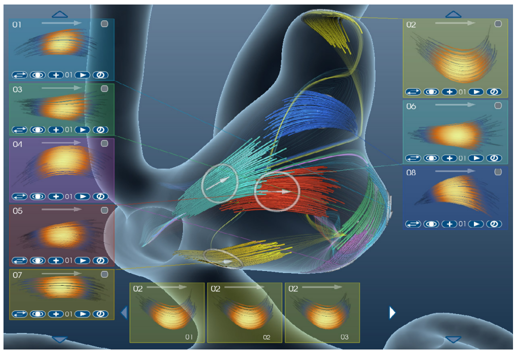

(d) Classfication

Figure 4: *Example workflow: At the initial state, all widgets are aligned at the left side (a). Also the timeline for the first flow pattern was enabled. Long streamlines can be included as spatial context (b). In (c), the user employed automatic camera positioning to center the 3D view and highlighted a single pattern. In (d) the user employed the overview widgets for binary classification.*

ticular pattern should be excluded from the current group, he/she can simply move the corresponding widget to the right side and vice versa.

Focus visualization. The visual inclusion of the vascular wall is important to comprehend the spatial flow characteristic. To convey the vascular shape without obstructing the internal flow, we employ a two-pass rendering: a white Fresnel shading is applied to the front faces and the back faces are rendered with a dark-blue color. They form a canvas for the brightly rendered streamlines while the surface normal-dependent Fresnel shading exhibit a higher opacity only at the visual border of the vasculature.

We provide two kinds of streamlines. Streamlines of the first kind have the propagation length L_p and correspond to the unrolled streamlines. They represent the local flow close to a given *CSR*. Streamlines of the second kind serve as an optional spatial flow overview. They have no fixed propagation length. The integration stops when a streamline intersects with the ostium plane (see Fig. 4(b)). To support differentiation when the global flow option is enabled, the original streamlines are represented by opaque stream tubes while the long streamlines are drawn as semi-transparent lines.

The streamline bundles of each *CSR* are individually colored. A semi-transparent ring represents each *CSR*. An arrow glyph at the center of this ring conveys the mean flow direction d_{mean} of each bundle. This direction is derived through averaging the directions of the first linear segments of all forward-integrated streamlines.

Streamline widget. To enable comparability between widgets, the unrolled streamlines are rotated such that their mean flow direction d_{mean} equals the screen space x-axis (see Fig. 5). This is visually conveyed by a left-to-right arrow at the top of the widget. As described in Section 6, the distance between the original streamlines and the *CSR* plane is employed as qualitative reliability indicator via color coding. The applied transfer function ranges from opaque-yellow (low distance - more trustworthy) over orange to a semi-transparent dark blue (high distance - less trustworthy).

To avoid ambiguity and reinforce visual correspondence

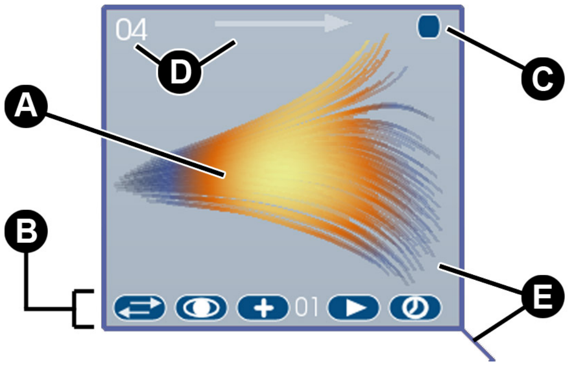

Figure 5: *Widget overview: The unrolled streamlines (A) are the central element. The button interface (B) provides functionality for (left-to-right): classification, viewpoint selection, manual and automatic time step selection, and timeline view activation. The mouse-over highlighting can be switched to permanent mode (C). To support comparison and identification, the widget provides the CSR ID, an arrow glyph of the mean flow direction (D) and has the same color as the streamline bundle in the 3D focus (E).*

between a widget and a corresponding 3D focus streamline bundle, every widget is labelled with a unique ID and the widget background and border are colored the same as the streamline bundle. Additionally, an equally colored screen space annotation line is drawn between the widget and the streamline bundle.

7.1. Interaction

The widget also contains a set of control elements that enable to trigger a set of interaction mechanisms that support classification, comparison and navigation (see Fig. 5).

Binary classification. By pressing the respective button, the widget is moved to the opposite side. If widgets are already present at this side, it is vertically integrated with respect to the rank of the corresponding *CSR*. The resulting classification is saved.

Highlighting. While the mouse pointer hovers over a widget, all streamline bundles, except for the corresponding one, are desaturated and their opacity is reduced. This also holds for the long streamlines if the global flow option is enabled. The corresponding flow pattern becomes visible with minimal obstruction and the user gets an immediate feedback where in the aneurysm it is located. Using the respective switch, it is also possible to enable a permanent highlighting.

Time step selection. Through the respective buttons, the user can choose the next time step or start and stop a continuous cycling through all given time steps. This can be convenient if the dataset contains a high number of time steps. The unrolled streamlines and the corresponding 3D streamlines are updated immediately. The updated unrolled streamlines are oriented with respect to d_{mean} of the first time step. Thus, directional changes over time become comprehensible. As a trade-off, the widget's arrow glyph is only correct for the first time step. However, it will still convey the basic flow direction as long as no full inversion occurs.

Timeline view. To obtain a temporal overview for a particular pattern, a timeline view can be enabled. This view is positioned below the 3D visualization and consists of horizontally arranged tiles. Each tile shows the unrolled streamlines for a particular time step. For comparability, they all are oriented according to the d_{mean} of the first time step.

Supported 3D navigation. To explore patterns in the 3D focus visualization, the user has to select an appropriate viewpoint by transforming the virtual camera. We provide a standard mouse-keyboard scheme; comparable to the ones provided in common 3D applications. However, for users with low experience in navigating 3D spaces, it is a tedious task to find a satisfying viewpoint.
Thus, we additionally provide the option to automatically transform the virtual camera with respect to the pattern of interest. A camera path is automatically generated. It results in an animation that consists of three phases (see Fig. 6).

- **Phase 1:** the camera view is centered with respect to the pattern of interest.
- **Phase 2:** the camera is moved above the pattern.
- **Phase 3:** the camera is rolled such that the orientation of the 3D streamline bundle is coincident with the unrolled streamlines.

The third phase primarily serves to reinforce the correspondence between unrolled and 3D streamlines.
For the first phase, the camera view is centred with respect to origin o_{CSR} of the *CSR* plane. This is animated through interpolation of the initial viewing vector and the new viewing vector $v_{new} = o_{CSR} - p_{cam}$, where p_{cam} is the current camera position. For all subsequent camera transformations, the viewing vector is updated to keep the view centered with respect to o_{CSR}.
The camera movement during the second phase is achieved through interpolation of the initial relative position vector $rp_{cam} = p_{cam} - o_{CSR}$ and the final relative position vector $rp'_{cam} = n_{CSR} \cdot d$, where n_{CSR} is the *CSR* plane's normal and d is the final distance to the *CSR* plane.
The actual camera position is calculated through $p_{cam} = o_{CSR} + (1-i) \cdot rp_{cam} + i \cdot rp'_{cam}$, where i is the interpolation parameter from 0 to 1. The distance d equals the aneurysm size indicator L_a. Thus, if the aneurysm is smaller the final camera position is closer to the aneurysm.
When the final position is reached, we employ ray casting at the center of the screen space to check if the pattern of interest is occluded by a part of the surrounding vasculature. If this is the case, d is iteratively halved, until the occlusion

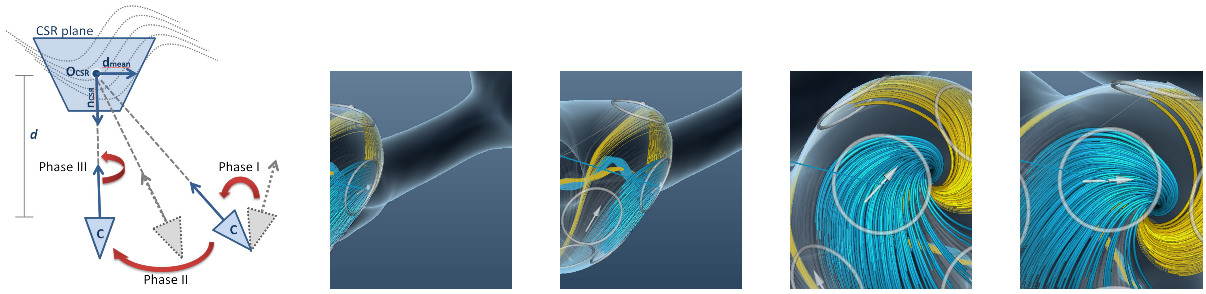

(a) Overview (b) Initial state (c) Phase 1 (d) Phase 2 (e) Phase 3

Figure 6: *Animation: In Phase 1 (c) the view is centered. In Phase 2 (d) the camera moves above the CSR plane and is then rolled with respect to d_{mean} (Phase 3 - (e)).*

is resolved.
The camera roll in the last phase of the animation is achieved through interpolating between the current up vector of the camera and the new up vector $u_{new} = n_{CSR} \times d_{mean}$. Thus, in the resulting view, the mean flow direction d_{mean} of the streamline bundle is coincident with the screen space x-axis. After the animation the user can manually transform the camera. The rotation pivot is set to equal o_{CSR}, thus it is straightforward to rotate the camera around the current flow pattern of interest.

8. Implementation and Datasets

The software prototype of the AmniVis-Explorer was implemented using the MeVisLab platform [RBH*11] and is based on the integrated VTK library [KSR*06]. As input data, it requires an unstructured grid containing the flow vector field for each time step. They are created from the output (EnSight format) of the Ansys *CFD* Solver. The polygonal vascular surface is extracted as boundary of the unstructured grid. As an additional input, an ostium plane mesh is generated [NDSP10].
Eight datasets, representing the variance of the datasets used in the planned study, are the basis of the informal user feedback: two datasets with multiple aneurysms, containing a total of five aneurysms, three datasets containing aneurysms with known rupture site, and three datasets of unruptured aneurysms (see Fig. 7). From each dataset, twenty time steps were extracted, evenly sampled forwards and backwards starting from the systolic peak. Depending on the resolution of the underlying simulation grid, the initial processing took from three to six seconds per *ROI* on a mid-class system (Core 2 Duo 3.16, 4GB RAM, nVidia GeForce 6000). The software-based streamline integration took most of the computation time. A hardware-based integration on a resampled, regular grid could enable real-time tracing. However, the current processing time is already feasible for practical application. After the processing the explorer allows for real-time interaction ($\geq$ 30 fps).

9. Informal User Feedback

The goal of the evaluation was to assess if the AmniVis-Explorer could support the tasks necessary for the study preparation. Thus, we wanted to learn, if the users (medical researchers) were able to explore the near-wall patterns and felt confident in providing a binary classification, based on the exploration. The interview involved three domain experts: two board-certified radiologists and a simulation expert who is involved in bio-medical flow research. All of them already worked with general visualization solutions like EnSight. Thus, they were able to compare our approach with common tools.
After a short introduction, they were asked to freely explore the flow patterns of a single aneurysm. Afterwards they were asked to provide a binary classification and justify their decision. Subsequently, they were asked to explore two aneurysms (side-by-side) with the additional task of comparing both. Afterwards, they were asked if they felt able to accomplish the tasks and if functionality was missing or expendable. To evaluate resulting changes in the explorer's design, the interviews were repeated a second time, after the new features were implemented.

Exploration and handling. All experts stated, that the automatically provided seeding regions mostly overlapped with the areas they would chose, based on surface curvature. However, two of them wanted to place additional seeding regions in flat areas, to gain more contextual information. During the exploration phase, we were able to observe a linkage between experience with 3D navigation and the way the user employed the 2D overview. The experienced user mainly focussed on the 3D representation and used the overview only for comparison. Less experienced users focused on the 2D overview for exploration and switched to the 3D view if they found the shape of the flow pattern to be not clearly represented in the 2D overview. For the temporal exploration, all provided approaches: step by step, cycling through time steps and an overview through the timeline view were employed by the experts. Since every expert preferred a differ-

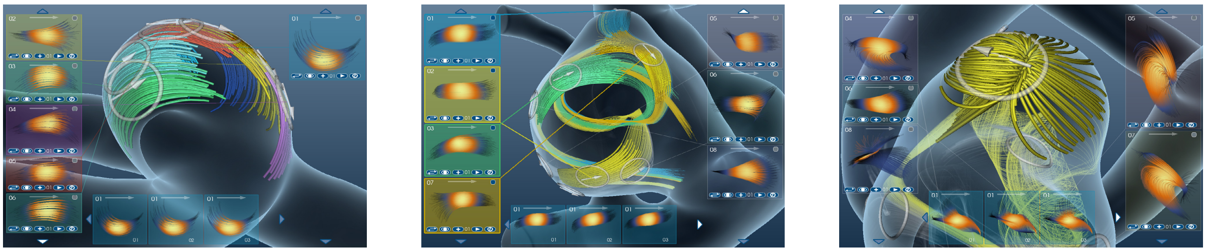

(a) MAS (b) Unruptured (c) Ruptured

Figure 7: *Example datasets: laminar flow in a smaller of multiple aneurysms (a), an expert classification of an unruptured aneurysm (b) and a ruptured aneurysm with view on the site of rupture (c).*

ent approach, no approach could be considered as obsolete. All three experts stated that the automatic viewpoint selection is a comfortable way to switch between different flow patterns in 3D. They also appreciated the similar orientation of the 2D and 3D representation after the camera positioning.

The feedback concerning the interface integration into the contextual overview was positive. All experts characterized the interface as easy to understand and emphasized that binary classification through widget arrangement is intuitive. When comparing two datasets the domain experts were satisfied with the side-by-side presentation. When asked if they prefer an integrated presentation, e.g. with two rows of widgets, one for each dataset, they refused and stated that no more complexity should be added to the interface.

Classification. Since a definition of salient flow features is not yet given, the classification results of this informal user feedback can only be interpreted implicitly. We observed that the experts divided the flow patterns based on complexity and stability. Patterns that exhibited strong changes over time or where stable over time but generally complex (e.g. swirl) were more likely to be considered salient. Except for minor differences (e.g. one user considered stable flow that diverges close to the *ROI* as salient) all classifications exhibited this basic structure with a broad overlap in-between the experts.

As an example, all experts defined flow patterns as salient that were close to the known site of rupture. It did not matter, whether the experts concentrated more on the 2D overview or the 3D focus visualization. The classification overlap was smaller, if the overall flow was more homogenous (e.g. mostly stable, laminar flow in an unruptured aneurysm). We assume this to be an indicator that no potentially salient patterns were present and the user started to focus on very small differences. However, all observations considering the classification have to be seen as preliminary, as the actual classes are yet to be defined in the future study.

Overall conclusion The informal feedback provides evidence that the explorer's design is suitable for the preparation of a qualitative study. The workflow (selection, exploration, classification) is completely supported; no features were stated to be missing. The explorer allowed for different exploration strategies while still leading to comparable results. Further application will show if the difference in strategy is interpersonal or if the increasing familiarity with this kind of data will lead to equalization. Once it was applied on a broader range of datasets, we also are able to quantify the classification variation and investigate possible systematic causes.

10. Outlook

In its current state, the explorer is designed for qualitative exploration and binary classification. However, the study preparation will lead to a deeper understanding about the kind of classes that are of interest. These insights can be included into the explorer's design. Hereby, the explorer will evolve into a tool that can be deployed for the actual study.

We are also currently investigating how pathlines or particle-based animations might be integrated, in order to enhance temporal exploration without sacrificing the ease of use and clarity of presentation. With more insight gained during the study, we are also planning to incorporate non-geometric, flow-based indicators (e.g. wall shear stress, oscillating shear index) for the automatic selection of *ROI*s.

Some of the explorer's features might be transferrable to other areas of applications. The interviewed radiologists expressed interest in applying a comparable explorer to data of aortic aneurysms, cardiovascular malformations and intracranial stenosis. We consider that the modular layout and general interaction schemes provide a good starting ground for extension and adaption of the AmniVis-Explorer.

Acknowledgments: We would like to thank U. Preim (Cardiac center Leipzig - department of radiology) for fruitful discussions and Fraunhofer MEVIS for providing the prototyping platform MeVisLab.

References

[CMWP11a] CEBRAL J., MUT F., WEIR J., PUTMAN C.: Association of hemodynamic characteristics and cerebral aneurysm rupture. *American Journal of Neuroradiology 32*, 2 (2011), 264–270. 1

[CMWP11b] CEBRAL J., MUT F., WEIR J., PUTMAN C.: Quantitative characterization of the hemodynamic environment in ruptured and unruptured brain aneurysms. *American Journal of Neuroradiology 32*, 1 (2011), 145–151. 1

[DJ97] DORAI C., JAIN A. K.: Cosmos-a representation scheme for 3d free-form objects. *Pattern Analysis and Machine Intelligence, IEEE Transactions on 19*, 10 (1997), 1115–1130. 2

[GNBP11] GASTEIGER R., NEUGEBAUER M., BEUING O., PREIM B.: The FLOWLENS: A Focus-and-Context Visualization Approach for Exploration of Blood Flow in Cerebral Aneurysms. *IEEE Transactions on Visualization and Computer Graphics (TVCG) 17*, 12 (2011), 2183–2192. 2

[KDM12] KADASI L., DENT W., MALEK A.: Cerebral aneurysm wall thickness analysis using intraoperative microscopy: effect of size and gender on thin translucent regions. *Journal of NeuroInterventional Surgery* (2012). 1

[KNG∗12] KÖHLER B., NEUGEBAUER M., GASTEIGER R., JANIGA G., SPECK O., PREIM B.: Surface-based seeding for blood flow exploration. In *Bildverarbeitung für die Medizin* (2012), pp. 81 – 86. 2

[KSR∗06] KOENIG M., SPINDLER W., REXILIUS J., JOMIER J., LINK F., PEITGEN H.: Embedding vtk and itk into a visual programming and rapid prototyping platform. In *Medical Imaging* (2006), Proc. of SPIE. 8

[LABFL09] LESAGE D., ANGELINI E. D., BLOCH I., FUNKA-LEA G.: A review of 3D vessel lumen segmentation techniques: Models, features and extraction schemes. *Medical Image Analysis 13*, 6 (December 2009), 819–845. 3

[MFW∗05] MENG H., FENG Y., WOODWARD S., BENDOK B., HANEL R., GUTERMAN L., HOPKINS L.: Mathematical model of the rupture mechanism of intracranial saccular aneurysms through daughter aneurysm formation and growth. *Neurological research 27*, 5 (2005), 459–465. 2

[MKB∗09] MOLYNEUX A., KERR R., BIRKS J., RAMZI N., YARNOLD J., SNEADE M., RISCHMILLER J., ET AL.: Risk of recurrent subarachnoid haemorrhage, death, or dependence and standardised mortality ratios after clipping or coiling of an intracranial aneurysm in the international subarachnoid aneurysm trial (isat): long-term follow-up. *Lancet neurology 8*, 5 (2009), 427. 1

[MLP∗10] MCLOUGHLIN T., LARAMEE R., PEIKERT R., POST F., CHEN M.: Over two decades of integration-based, geometric flow visualization. *Computer Graphics Forum 29*, 6 (2010), 1807–1829. 2

[MNTP07] MÜHLER K., NEUGEBAUER M., TIETJEN C., PREIM B.: Viewpoint Selection for Intervention Planning. In *IEEE/Eurographics Symposium on Visualization (EuroVis)* (2007), pp. 267–274. 2

[NDSP10] NEUGEBAUER M., DIEHL V., SKALEJ M., PREIM B.: Geometric reconstruction of the ostium of cerebral aneurysms. In *Proc. of VMV* (2010), pp. 307–314. 3, 8

[NGB∗09] NEUGEBAUER M., GASTEIGER R., BEUING O., DIEHL V., SKALEJ M., PREIM B.: Map Displays for the Analysis of Scalar Data on Cerebral Aneurysm Surfaces. *Computer Graphics Forum 28 (3)* (2009), 895–902. 2

[NJB∗11] NEUGEBAUER M., JANIGA G., BEUING O., SKALEJ M., PREIM B.: Anatomy-Guided Multi-Level Exploration of Blood Flow in Cerebral Aneurysms. *Computer Graphics Forum 30(3)* (2011), 1041–1050. 2

[PPG∗08] PETZ C., PROHASKA S., GOUBERGRITS L., KERTZSCHER U., HEGE H.-C.: Near-wall flow visualization in flattened surface neighborhoods. In *Simulation and Visualization* (2008), SCS Publishing House, pp. 93–105. 2

[PVH∗03] POST F., VROLIJK B., HAUSER H., LARAMEE R., DOLEISCH H.: The state of the art in flow visualisation: Feature extraction and tracking. *Computer Graphics Forum 22*, 4 (2003), 775–792. 2

[RBH∗11] RITTER F., BOSKAMP T., HOMEYER A., LAUE H., SCHWIER M., LINK F., PEITGEN H.: Medical image analysis. *Pulse, IEEE 2*, 6 (nov.-dec. 2011), 60 –70.

[RPP∗09] ROSANWO O., PETZ C., PROHASKA S., HEGE H., HOTZ I.: Dual streamline seeding. In *Proc. of IEEE PacificVis' 09.* (2009), pp. 9–16. 2

[RRW∗08] RAYMOND J., ROY D., WEILL A., GUILBERT F., NGUYEN T., MOLYNEUX A., FOX A., JOHNSTON S., COLLET J., ROULEAU I., ET AL.: Unruptured intracranial aneurysms and the trial on endovascular aneurysm management (team): The principles behind the protocol. *Journal of Vascular and Interventional Neurology 1*, 1 (2008), 22. 1

[Sch97] SCHÖBERL J.: Netgen an advancing front 2d/3d-mesh generator based on abstract rules. *Computing and Visualization in Science 1* (1997), 41–52. 3

[TMWS12] TAO J., MA J., WANG C., SHENE C.-K.: A unified approach to streamline selection and viewpoint selection for 3d flow visualization. *IEEE Transactions on Visualization and Computer Graphics*, Epub ahead of print (2012). 2

[vPBB∗10] VAN PELT R., BESCÓS J., BREEUWER M., CLOUGH R., GROLLER M., TER HAAR ROMENIJ B., VILANOVA A.: Exploration of 4d mri blood flow using stylistic visualization. *Visualization and Computer Graphics, IEEE Transactions on 16*, 6 (2010), 1339–1347. 2

[XNT∗11] XIANG J., NATARAJAN S., TREMMEL M., MA D., MOCCO J., HOPKINS L., SIDDIQUI A., LEVY E., MENG H.: Hemodynamic–morphologic discriminants for intracranial aneurysm rupture. *Stroke 42*, 1 (2011), 144–152. 1

[YD04] YOSHIDA H., DACHMAN A. H.: Computer-aided diagnosis for CT colonography. In *Seminars in Ultrasound, CT, and MRI* (2004), vol. 25, Elsevier, pp. 419–431. 2, 4